Geophysical Research Letters

RESEARCH LETTER
10.1029/2024GL109367

Probability of Firn Aquifer Presence in Antarctica by Combining Remote Sensing and Regional Climate Model Data

V. Di Biase[1], P. Kuipers Munneke[1], S. B. M. Veldhuijsen[1], S. de Roda Husman[2], M. R. van den Broeke[1], B. Noël[3], L. G. Buth[4], and B. Wouters[2]

[1]Department of Physics, Institute for Marine and Atmospheric Research, Utrecht University, Utrecht, The Netherlands, [2]Department of Geoscience & Remote Sensing, Delft University of Technology, Delft, The Netherlands, [3]Laboratoire de Climatologie et Topoclimatologie, University of Liège, Liège, Belgium, [4]Alfred Wegener Institute, Helmholtz Centre for Polar and Marine Research, Bremerhaven, Germany

Key Points:

- An innovative aquifer detection method, combining satellite and regional climate model data, is applied to Antarctica
- The evaluation of the methodology in Greenland, showing 91% correspondence, suggests good adaptability for Antarctica
- The Antarctic Peninsula stands out as the only region with high aquifer probability; in the rest of Antarctica, the likelihood is low

Supporting Information:

Supporting Information may be found in the online version of this article.

Correspondence to:

V. Di Biase,
v.dibiase@uu.nl

Citation:

Di Biase, V., Kuipers Munneke, P., Veldhuijsen, S. B. M., de Roda Husman, S., van den Broeke, M. R., Noël, B., et al. (2024). Probability of firn aquifer presence in Antarctica by combining remote sensing and regional climate model data. *Geophysical Research Letters*, *51*, e2024GL109367. https://doi.org/10.1029/2024GL109367

Received 21 MAR 2024
Accepted 24 JUL 2024

Abstract Despite in-situ observations of perennial firn aquifers (PFAs) at specific locations of the Antarctic ice sheet, a comprehensive continent-wide mapping of PFA distribution is currently lacking. We present an estimate of their distribution across Antarctica in the form of a probability assessment using a Monte Carlo technique. Our approach involves a novel methodology that combines observations from Sentinel-1 and Advanced SCATterometer (ASCAT) with output from a regional climate model. To evaluate our method, we conduct an extensive comparison with Operation Ice Bridge observations from the Greenland Ice Sheet. Application to Antarctica reveals high PFA probabilities in the Antarctic Peninsula (AP), particularly along its northern, northwestern, and western coastlines, as well as on the Wilkins, Müller, and George VI ice shelves. Outside the AP, PFA probability is low, except for some locations with marginally higher probabilities, such as on the Abbot, Totten, and Shackleton ice shelves.

Plain Language Summary We explore the presence of subsurface water storage within the firn layer in Antarctica, known as perennial firn aquifers (PFA), using a new method that combines satellite data and climate models. These PFAs, previously identified in Greenland, store and transmit meltwater, and could influence ice-sheet behavior. Our study maps the likelihood of PFAs across Antarctica, finding high probabilities along the Antarctic Peninsula's northern and western coasts, as well as on specific ice shelves. Outside this region, PFAs are unlikely, except for a few spots with somewhat enhanced probability on Abbot, Totten, and Shackleton ice shelves. This inventory enhances our understanding of Antarctic hydrology and has broader implications for understanding ice-sheet dynamics.

1. Introduction

The polar ice sheets of Antarctica and Greenland are undergoing substantial changes due to global climate change (Ming et al., 2021). Among the various processes shaping these ice sheets, PFAs stand out as a relatively recent discovery (Forster et al., 2014) that merit close examination. PFAs have considerable influence over the thermal state of the ice sheets, and harbor the potential to impact ice dynamics and stability through mechanisms such as meltwater-induced hydrofracturing (Brangers et al., 2020; Forster et al., 2014; Fountain & Walder, 1998; Humphrey et al., 2012; Kuipers Munneke et al., 2014; Miège et al., 2016; Montgomery et al., 2020; Nienow et al., 2017; Phillips et al., 2010; Poinar et al., 2017). PFAs have also been shown to influence meltwater discharge (O. Miller et al., 2018; Montgomery et al., 2020). With rising global temperatures driving enhanced meltwater production across polar ice sheets (Siegert et al., 2019; Trusel et al., 2015), understanding the pathways of meltwater—a key factor in ice shelf disintegration (Scambos et al., 2000; van den Broeke, 2005; Scambos et al., 2009; Gilbert & Kittel, 2021)—highlights the significance of PFAs.

Characterized by subsurface liquid water storage, PFAs form under specific conditions of both high melt and high accumulation rates (Brils et al., 2024; Kuipers Munneke et al., 2014). PFAs were initially detected within mountain glaciers (Fountain, 1989; Schneider, 1999), with subsequent identification in Greenland (Forster et al., 2014) and Svalbard (Christianson et al., 2015). Since then, various methodologies have been applied to detect and analyze these PFAs, including in situ measurements through borehole drilling (MacDonell et al., 2021; Montgomery et al., 2020), ground and airborne radar data (Chu et al., 2018; Forster et al., 2014; Miège

et al., 2016), and satellite remote sensing employing Sentinel-1 (S1) C-band radar imagery (Brangers et al., 2020) and Soil Moisture Active Passive (SMAP) L-band brightness temperature measurements (J. Z. Miller et al., 2020). However, their existence and characteristics in Antarctica remain poorly known and spatially limited. Efforts to study PFAs in Antarctica have included in situ investigations (MacDonell et al., 2021), Ground Penetrating Radar (GPR) assessments (Montgomery et al., 2020; Simões et al., 2004; da Rosa et al., 2014), and simulations using regional climate model outputs (van Wessem et al., 2021). Montgomery et al. (2020) detected an extensive perennial firn PFA on Wilkins Ice Shelf through drilling and GPR techniques, also confirmed by locally extended Operation Ice Bridge (OIB) Multichannel Coherent Radar Depth Sounder (MCoRDS) data (Miège et al., 2020).

Unlike Greenland, a comprehensive assessment of PFA presence in Antarctica using OIB data remains unavailable at present. As suggested by Miège et al. (2016), such mapping necessitates the concurrent utilization of MCoRDS and Accumulation Radar (AR) data. While MCoRDS data are widely accessible across Antarctica for selected years and regions, integrating them with AR data presents more challenges, both in terms of temporal and spatial limitations.

To leverage the current methodologies in Antarctica, we employ an innovative approach that combines multiple satellite data sets and model output. Central to this method is the fusion of an S1 PFA detection technique, based on the distinctive absorptive properties of liquid water (Stiles & Ulaby, 1980), with data from ASCAT, widely used for monitoring surface melt phenomena across both Greenland (Shang et al., 2022) and Antarctica (Bevan et al., 2018; de Roda Husman et al., 2022). Furthermore, we incorporate regional climate modeling data, which offer information on snowfall accumulation and melt rates - crucial to predict the presence of PFAs (Kuipers Munneke et al., 2014). Our approach involves the combination of these diverse data sets through a Monte Carlo (MC) methodology, a widely utilized probabilistic technique across various scientific disciplines (Dunn & Shultis, 2011), to assess the probability distribution of specific variables under investigation. By addressing the complexities of calibrating remote sensing results in the Antarctic, this versatile integration helps to average out errors from single predictors and accounts for potential false detections, thus enhancing the robustness and accuracy of our analysis. The outcome of this process is a probability map of PFA presence, and shows the spatial variability across the study area at a high 2 km spatial resolution. Our results are evaluated and calibrated using existing OIB PFA mapping both in Greenland, which provides extensive and detailed coverage, and on Wilkins Ice Shelf.

The present study operates within the context of limited field observations, acknowledging that the vast and remote nature of the Antarctic continent poses substantial logistical challenges for direct on-site investigations. In the absence of robust continent-wide observations, this novel approach provides a nuanced understanding of the distribution and potential extent of PFAs in Antarctica.

2. Materials

To identify the presence of PFAs, we leverage three independent data sets - S1, ASCAT, and RACMO2.3p2 - spanning from 2017 to 2021. These data sets, each highlighting a different indicator for PFA existence, serve as input for a MC methodology used to generate an Antarctica PFA heat map. This section introduces the three data sets utilized for input, complemented by a fourth data set - OIB - employed specifically for evaluation.

2.1. Sentinel-1

Copernicus S1 data are exploited to distinguish potential PFA from non-PFA locations. This distinction relies on monitoring how radar backscatter evolves after the melt season has finished (Brangers et al., 2020). S1 Synthetic Aperture Radar (SAR) C-band (5.405 GHz) radar backscatter measurements (σ^0_{HH}, in dB) are used in the present work. Level-1 Ground Range Detected (GRD) images, Extra-Wide Swath Mode, are exploited for the period 2017 to 2021. In Antarctica and Greenland, data for both horizontal-horizontal (HH) and horizontal-vertical (HV) polarizations are accessible, with a swath of 410 km and a spatial resolution of 20 × 40 m. As in Brangers et al. (2020), comparable outcomes are derived from the analysis of HH and HV data independently. Consequently, only the results of HH measurements (σ^0_{HH}) are presented here. Data have been preprocessed via the Python API of the Google Earth Engine and aggregated to 1 km by linear scale averaging (Gorelick et al., 2017). The processed data was then projected onto the global cylindrical equal-area scalable Earth Grid resolution version 2 (EASE-2) (Brangers et al., 2020; Brodzik et al., 2012). The S1 constellation (A/B) offers a 6-day repeat

cycle. For each satellite pass within one cycle, identified by its relative orbit number (RON), the geometry of the orbiting satellite with respect to the Earth's surface is different, which influences backscatter measurements and results in a RON-specific bias. The bias is assessed on a pixel-wise basis (Lievens et al., 2019), and removed for all RONs with at least 50 data points.

2.2. ASCAT

ASCAT observations are used as an indicator for the duration of the melt season. ASCAT operates in C-band (5.255 GHz) and antennas are vertically polarized only. In the southern hemisphere, ASCAT passes in the morning and in the evening. The 4.45 km enhanced resolution product is used, which was developed by the NASA Scatterometer Climate Record Pathfinder Project (available at: http://www.scp.byu.edu, last accessed on 24 May 2023) (Long et al., 1993).

2.3. RACMO2.3p2

PFAs are typically situated in regions characterized by moderate to high surface melt and elevated accumulation rates (Brils et al., 2024; Kuipers Munneke et al., 2014; van Wessem et al., 2021). Such climate conditions are estimated from regional climate model data, including annual cumulative surface mass balance (SMB), accumulation and melt data. These data serve as indicators of PFA presence (Kuipers Munneke et al., 2014). These values are statistically downscaled to 2 × 2 km from the output of the regional climate model RACMO2.3p2 (27 × 27 km resolution) (Noël et al., 2023) in the Antarctic region. For the Greenland Ice Sheet, data at a resolution of 1 × 1 km is employed, statistically downscaled from the output of RACMO2.3p2 at 5.5 × 5.5 km (Noël et al., 2019).

2.4. Operation IceBridge

First, our method is trained and evaluated using OIB PFA observations in Greenland from 2010 to 2017, which offer comprehensive mapping of PFAs (Miège et al., 2016). Second, given the lack of comprehensive PFA observations in Antarctica, we calibrate the thresholds for this region using OIB MCoRDS data from Wilkins Ice Shelf, collected in 2014 (Miège et al., 2020). This data set serves as an indicator of PFA presence, allowing us to fine-tune the method's thresholds and assess its validity in this region.

3. Method

In this study, our focus extends to two primary regions: Antarctica, where the method is applied to gain insights into the probability of PFA presence, and Greenland, chosen for method evaluation. The algorithm's flowchart is presented in Figure 1.

The data sets from S1, ASCAT, and RACMO2.3p2 (Section 2) are used as inputs for a MC method. The suite of tests for analyzing these input variables is described here.

As an initial step, blue-ice areas are excluded from the entire data set using the mask of Hui et al. (2014), due to their backscatter responses resembling those found in PFA locations (de Roda Husman et al., 2022). For the remaining pixels, a suite of tests is initiated, which can be classified into two satellite-based tests (hereafter referred to as *S1* and *ASCAT* tests, respectively) and two model-based tests (hereafter referred to as *accumulation* and *melt* tests, respectively). The outcome of these four tests will jointly define the probability of PFA presence. Their weights, referring to the influence assigned to each of these tests in determining the overall outcome of the MC algorithm, are hereafter referred to as w_{S1}, w_{ASCAT}, w_{acc}, w_{melt}, respectively. For each iteration of the algorithm, these weights are randomly selected from values ranging from 0% to 50% (so that the median values are close to 25%, corresponding to the case in which the tests have equal weight). A scaling factor is applied so that the sum of the weights equals 1.

The MC algorithm (Figure 1) is initially applied to single-year data, generating yearly heat maps. To enhance stability and reduce annual variability, we average estimated probabilities for each pixel over a 5-year period. This process minimizes the impact of year-specific anomalies, providing a more reliable and robust overall assessment, diminishing random uncertainties and contributing to a statistically robust outcome. MC simulations are executed, for each of the considered years, for 10,000 iterations. Even with a lower number of iterations, the method converges to the presented results.

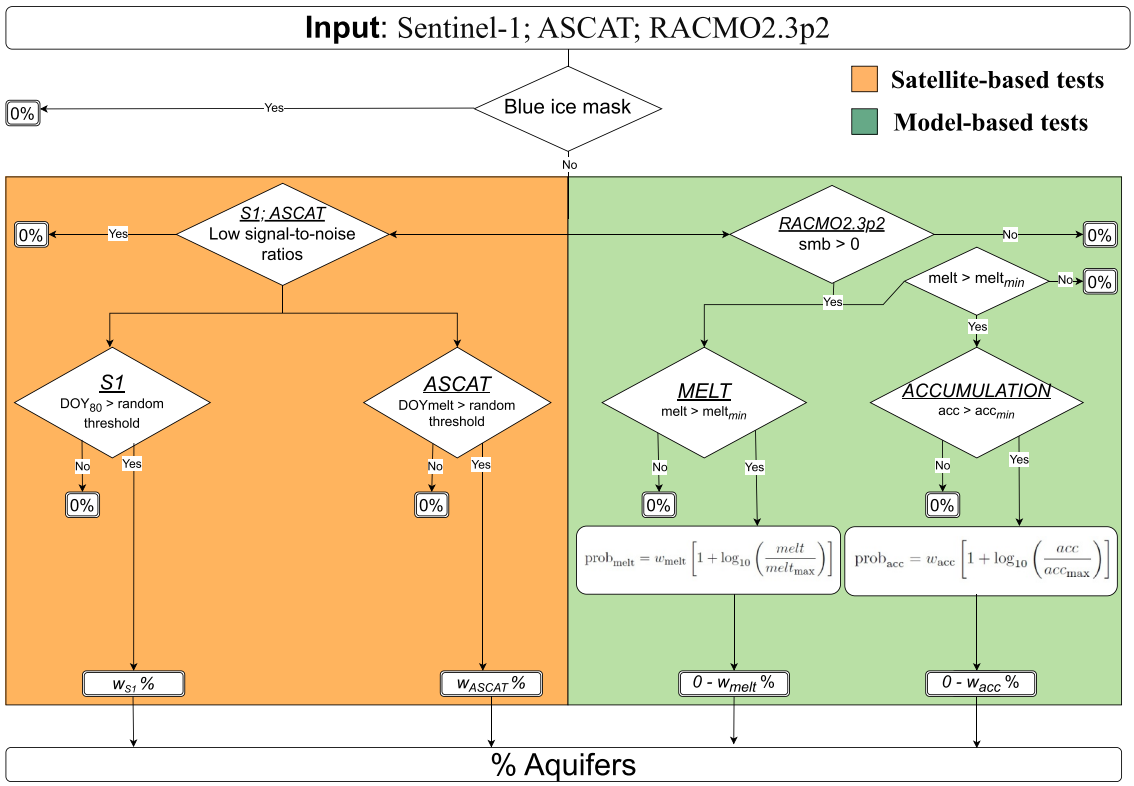

Figure 1. MC algorithm for PFA probability map.

Separate iterations of the algorithm are finally conducted to assess the impact of the four individual tests on the final result. The findings are discussed in Sect. 6; see also in Supporting Information S1, Figure S3.

3.1. Satellite Tests

For the two MC satellite-based tests, we implement an initial filter to mask pixels characterized by low signal-to-noise ratios. The identification of these pixels is determined by evaluating the following conditions (de Roda Husman et al., 2022; Zheng & Zhou, 2020).

- The mean backscatter intensity during winter (June—August) is below −14 dB;
- The minimum backscatter intensity during winter is less than 3 dB smaller than the minimum backscatter intensity during summer (December—February).

In the two tests described below, certain thresholds need to be defined. These are initially derived in Greenland to train the algorithm.

3.1.1. Sentinel-1

The backscatter signal from microwave radar decreases as snow becomes wetter due to increased absorption and altered scattering by liquid water (Shi & Dozier, 1992; Stiles & Ulaby, 1980; Tsai et al., 2019). In areas with minimal meltwater retention, refreezing post-melt season leads to an increase in σ_{0HH}, returning to pre-melt levels within days or weeks. PFAs slow down refreezing due to latent heat, causing a delayed radar backscatter increase (Brangers et al., 2020; Humphrey et al., 2012; Kuipers Munneke et al., 2014; Phillips et al., 2010). The limited C-band penetration (Dall et al., 2001; Rignot et al., 2001) may not directly sense the PFA water table, however this delayed refreezing of water in the unsaturated firn layer above the PFA creates a distinctive backscatter signal, serving as a proxy for PFA detection. Brangers et al. (2020) uses a backscatter intensity difference threshold at fixed times to detect PFAs in Greenland. This work adapts Brangers' approach by observing the recovery time of σ_{0HH} to pre-melt values (Figure S1 in Supporting Information S1). The day of the year when the backscatter reaches 80% of the pre-melt value is referred to as DOY_{80}. This date is here used as a threshold for differentiating

between regions without PFAs and those with PFAs. In the MC algorithm, the *S1* test involves the following steps.

- Identification of the study area: We start by selecting regions in Greenland where there is an overlap between S1 data and OIB PFAs, establishing this region as the study area for subsequent threshold generation (Figure S2 in Supporting Information S1).
- Creation of a DOY_{80} matrix: A matrix representing DOY_{80} values for the selected study area across all analyzed years is created.
- Determination of normal distribution: We identify the Gaussian distribution of the sample. After excluding outliers, the mean $(\mu_{DOY_{80}})$ and standard deviation $(\sigma_{DOY_{80}})$ are estimated as 99 and 21, respectively (Figure S2 in Supporting Information S1).
- Random threshold generation: Random values, referred to as DOY_{80} random thresholds, are then extracted from this normal distribution.
- Boolean matrix generation: For each extracted random threshold, a Boolean matrix - analogous to the DOY_{80} matrix - is generated. This matrix identifies pixels with DOY_{80} values equal to or exceeding the randomly generated threshold.
- Passing the test: In each iteration, the test is passed by pixels whose DOY_{80} is higher than the extracted threshold.
- Threshold variation: Throughout 10,000 iterations, the above three steps are repeated. The threshold value dynamically changes while adhering to normal distribution constraints.
- Tallying and weighted average: For each pixel, 'true' instances are recorded, and the corresponding percentage is calculated, directly yielding the probability for every pixel. The resulting matrix signifies the percentage of favorable cases, which serves as the basis for a weighted average. This average, determined by randomly assigned weights in each iteration, reflects the overall contribution of pixels passing the *S1* test, represented by the extracted weight w_{S1}.

3.1.2. ASCAT

The present *ASCAT* test serves as an indicator for the duration of the melting season. To ensure the captured data corresponds to the end of the melt season, the study focuses exclusively on afternoon (6 p.m.) observations, as morning observations (6 a.m.) exhibit less melting (de Roda Husman et al., 2022; Trusel et al., 2012). The melt detection algorithm proposed by Ashcraft and Long (2006) is implemented, assuming the presence of melt when the backscatter intensity falls below the annual winter mean by a threshold of 3 dB. Melt periods need to encompass four consecutive observations, with at least three out of the four observations indicating melt. Individual melt days are excluded, as a longer duration of melting is deemed necessary for PFA formation. The last day of melt within the final selected melt period represents the "end of the melt season" (DOY_{melt}). In the MC algorithm, the same seven steps as for S1 (Section 3.1.1) are taken to determine w_{ASCAT}, where DOY_{melt} now replaces DOY_{80}. In the determination of the normal distribution (Figure S2 in Supporting Information S1), the mean $(\mu_{DOY_{melt}})$ and standard deviation $(\sigma_{DOY_{melt}})$ are estimated as 87 and 22, respectively.

3.2. RACMO3.2p2 Tests

To ensure the inclusion of suitable areas for PFA formation, an initial filtering step is applied to the input RACMO3.2p2 data. This step is guided by the assumption that PFAs are, by definition, not expected to form in ablation areas where runoff and/or sublimation exceeds accumulation. Accordingly, pixels with negative annual SMB values are masked.

The MC algorithm involves two distinct tests, *accumulation* and *melt*. Employing a progressive thresholding approach in each test, we assign probabilities of PFA presence within a range spanning from 0% to the weight extracted for the respective test.

3.2.1. Accumulation

PFAs are frequently observed in regions characterized by sufficient annual accumulation, along with moderate to high melt rates (Kuipers Munneke et al., 2014). To refine our analysis, we apply a restriction to the *accumulation* test, limiting its application to pixels with melt values exceeding a minimum melt threshold of 40 mm w e yr^{-1}. For the assessment of the *accumulation* test, we employ a progressive thresholding approach expressed by:

$$\text{prob}_{\text{acc}} = w_{\text{acc}}\left[1 + \log_{10}\left(\frac{acc}{acc_{\text{max}}}\right)\right] \quad (1)$$

In this equation, prob_{acc} is the probability estimated for the *accumulation* test in each iteration; *acc* represents the annual accumulation value for each pixel, with the maximum accumulation limit set at $acc_{\text{max}} = 2000$ mm w e yr^{-1}. The threshold value is calibrated based on the findings of van Wessem et al. (2021), which indicate that characteristic accumulation values in regions with PFA presence typically exceed 1000 mm w e yr^{-1}. Due to the progressive nature of this threshold test, a maximum value — set at double this amount — is chosen. The choice of acc_{max} threshold was further tested by using different values based on distribution estimates, but these adjustments led to worse results (not shown), confirming that our original thresholds were more effective. Pixels with accumulation below 200 mm w e yr^{-1} have 0% probability, while those above 2000 mm w e yr^{-1} have probability w_{acc}.

3.2.2. Melt

Likewise, we use a progressive thresholding approach for the assessment of the *melt* test:

$$\text{prob}_{\text{melt}} = w_{\text{melt}}\left[1 + \log_{10}\left(\frac{melt}{melt_{\text{max}}}\right)\right] \quad (2)$$

where $\text{prob}_{\text{melt}}$ is the probability estimated for the *melt* test in each iteration; *melt* represents the annual melt value for each pixel, with the maximum melt limit set at $melt_{\text{max}} = 400$ mm w e yr^{-1}. The threshold value is calibrated based on the findings of van Wessem et al. (2021), which indicate that characteristic surface melt values in regions with PFA presence typically exceed 200 mm w e yr^{-1}. Due to the progressive nature of this threshold test, a maximum value — set at double this amount — is chosen. The choice of thresholds has been further tested, yielding worse results (not shown). Pixels with melt below 40 mm w e yr^{-1} have 0% probability, while those above 400 mm w e yr^{-1} have probability w_{melt}.

4. Method Evaluation and Calibration

Our methodology - using input data spanning from 2017 to 2021 - is implemented on Greenland using OIB data spanning from 2010 to 2017 and then calibrated on Wilkins Ice Shelf using MCoRDS data derived in 2014. Despite operating within distinct time frames, the evaluation assumes steady-state behavior in PFAs, not considering transient phenomena observed by Miège et al. (2016). MC results outside OIB PFA areas are excluded.

4.1. Evaluation on the Greenland Ice Sheet

The evaluation, shown in Figure 2, includes a map (Figures 2a–2d)), histograms (Figures 2e and 2f)), and probability distributions (Figures 2g and 2h)) of MC probabilities in comparison to OIB flightiness without PFA detections (e-g), and those with detected PFAs (f-h).

Figure 2h, reveals that over 91% of pixels within OIB PFA areas match MC probabilities above 50%. In non-PFA areas, most MC simulations show probabilities below 10%, with approximately 95% falling below 50%. We consider a MC probability of 50% as the minimum threshold for effective PFA discrimination.

In Figure 2a, we present a comparison between MC-detected PFAs (2017–2021) and OIB PFAs (2010–2017) in Greenland; close views are provided for specific regions: southwest (b), northwest (c), and southeast (d). Areas where MC probabilities exceed 50% and align with OIB PFAs are highlighted in green, while OIB PFAs are represented by green plus red areas. Among non-PFA locations identified by OIB, 4% are false positives (identified as PFAs by MC, indicated by yellow lines), and 9% are false negatives (red pixels). False positives tend to concentrate around the boundaries of detected OIB PFA areas, possibly influenced by differences in time periods and spatial resolutions between the two detection systems; possibly, this result aligns with reported PFA expansion in southwestern Greenland (Horlings et al., 2022). A PFA heat map for Greenland, generated with MC, is shown in Figure S4 in Supporting Information S1.

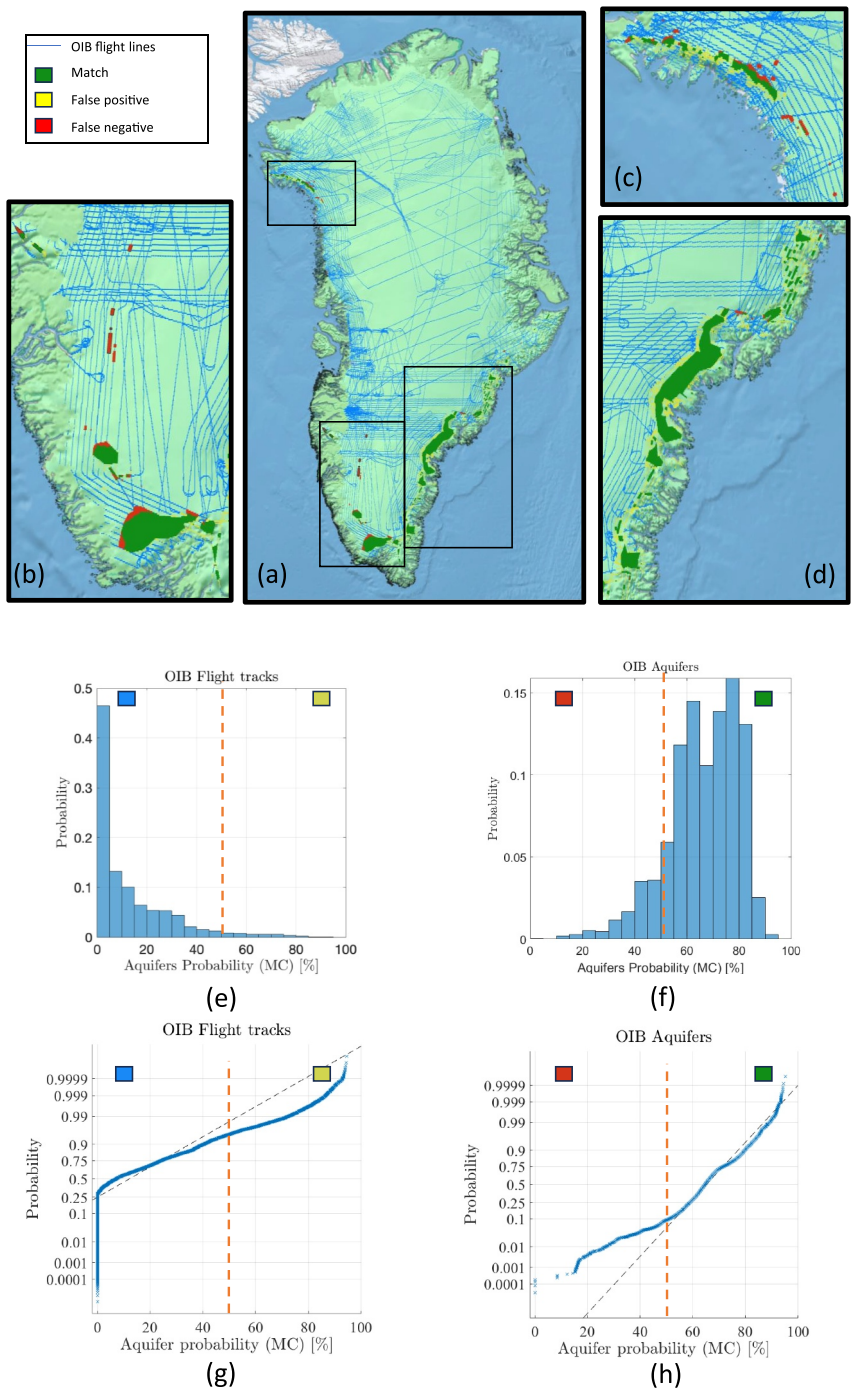

Figure 2. (a–d): PFA locations according to OIB and MC (e–f) histograms and (g–h) probability distributions of the MC probabilities with respect to the OIB flightlines (left panels) and OIB PFAs (right panels). The color scheme across all figures is as follows: dark green indicates a PFA match between OIB and MC, yellow denotes false positives, red indicates false negatives, and blue represents OIB flight lines where neither OIB nor MC PFAs are detected. The dotted orange line represents the 50% threshold chosen to discriminate PFAs by non PFA locations.

4.2. Evaluation and Calibration on Wilkins Ice Shelf

MCoRDS radar maps the depth of the water table, and 2014 data over Wilkins Ice Shelf (Miège et al., 2020) serve as indicators of PFA locations. These data are used to fine-tune the thresholds derived in the Greenland evaluation. Mean ($\mu_{\mathrm{DOY}_{melt}}$ and $\mu_{\mathrm{DOY}_{80}}$) and standard deviation ($\sigma_{\mathrm{DOY}_{melt}}$ and $\sigma_{\mathrm{DOY}_{80}}$) are estimated as 101 and 119 for

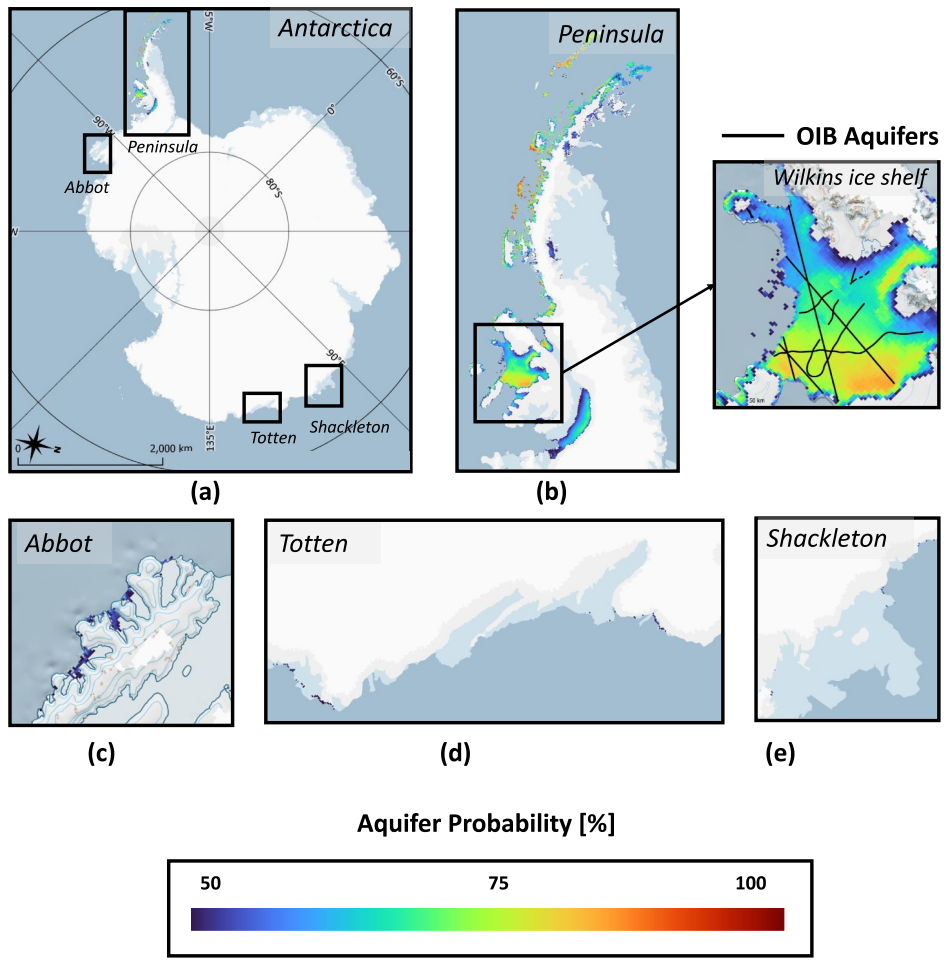

Figure 3. Antarctica PFAs heat map (a), generated with data spanning 2017–2021, showing areas with PFA concentrations having a probability above 50%. (b) High probability of PFAs found within the Antarctic Peninsula (AP), with a close-up view of the Wilkins Ice Shelf. The black lines indicate OIB flight paths where a water table was detected by MCoRDS on 16 November 2014. Sporadic occurrences of PFAs are also observed in selected ice shelves such as Abbot (c), Totten (d), and Shackleton (e).

DOY_{melt} and 99 and 22 for DOY_{80} as derived in Sections 3.1.1 and 3.1.2, while model testing uses consistent thresholds (Section 3.2). The adaptation achieves a 97% detection rate of PFAs identified by OIB data (Figure 3c), showing the method's robustness across different regions. The thresholds estimated in Greenland were also tested on Wilkins Ice Shelf, resulting in a minor decrease in performance of approximately one percentage point. It demonstrates that our method is robust for any geographical location. Therefore, Wilkins' thresholds have been applied across the entirety of Antarctica.

5. Results: Antarctica PFA Heat Map

The MC algorithm used for this study results in a comprehensive PFA heat map for Antarctica at 2 × 2 km resolution, shown in Figure 3a. The analysis reveals that the vast majority of PFAs are concentrated in the AP (Figure 3b). The areas within the AP with significantly elevated probabilities of having PFAs are mainly situated along the northern, northwestern, and western coastlines of the AP. Furthermore, there are also high probabilities on the Wilkins (Figure 3b), Müller and George VI ice shelves. In regions such as the high-elevation zone in the central AP, or the Larsen C Ice Shelf which experiences significant snowmelt but comparatively lower accumulation rates - conditions typically unsuitable for PFA formation (Kuipers Munneke et al., 2014) - PFA

probability is low. Outside of the AP, PFA probability is low, with the exception of slightly elevated probabilities (i.e., 50%–55%) on some ice shelves, for example, Abbot, Totten, Shackleton (Figures 3c, 3d and 3e)).

The individual results - showing the PFA probability for each of the four tests in the selected areas with total occurrence above 50% - are shown in Figure S3 in Supporting Information S1.

6. Discussion

Acknowledging the potential of a binary option in PFA detection (Brangers et al., 2020; J. Z. Miller et al., 2020), we favor a probabilistic approach due to the complexities of calibrating and validating remote sensing methodologies in the unique Antarctic environment, making our final map less sensitive to the limitations of any single approach.

First, we investigate the importance of each test to the final results. This examination enriches our understanding of the robustness and reliability of the chosen tests. Within the Greenland Ice Sheet, we randomly leave out individual tests and data sets to assess their impact on the final result (Table S1 in Supporting Information S1). These tests highlight how the combination of the chosen tests maximizes overall performance, considering false positives, false negatives, and matches. By relying on a varied set of tests over multiple years, the approach also accommodates potential false detections in individual annual tests, offering a comprehensive approach. Moreover, the tests reveal the method's robust performance, even when excluding one of the satellite inputs. This highlights the approach's versatility and applicability in scenarios involving satellite failure or unavailability. Such adaptability positions this method as a reliable option for future applications.

Second, we complement the analysis above with the partial results of each of the four tests individually (Figure S3 in Supporting Information S1): the combination of all tests proves valuable in balancing their respective positive and negative impacts. The *melt* test emerges as the most impactful, preventing a deterioration of confirmed positives without it. While some chosen thresholds may be perceived as too rigid and others a bit lenient, each exerts a dampening effect on potential false positives and negatives.

All the thresholds used in the MC are further tested: slight variations in the S1 and ASCAT thresholds result in only minor changes to the final results, while variations in the RACMO2.3 thresholds have a slightly greater impact. This is because they make the two model-driven tests too influential, and any under- or overestimations can no longer be balanced within the MC. Therefore, fixed thresholds that demonstrate optimal performance in this context are selected.

As a final point of discussion, we look at locations with in situ confirmed PFAs presence. There is a PFA at Wanda Glacier (Simões et al., 2004), and our method aligns with a 61% probability. At Müller (MacDonell et al., 2021) and Wilkins Ice Shelves (Montgomery et al., 2020), two other locations with confirmed PFA presence, our method yields a probability of 74% and 79%, respectively. Moving to the southern part of the George VI ice shelf, where radar measurements previously disclosed ice thickness up to hundreds of meters without water reflection (Smith, 1972), our methodology reveals positive outcomes within the range of 50%–60%. Intense melt events in certain years during the analysis (Banwell et al., 2021), captured by both *ASCAT* and the *melt* test, contribute to this result. This, coupled with high accumulation, leads to the prediction of a considerable PFA area. However, this outcome stands as an isolated case, as evident from the low incidence of false positives in the presented assessment.

7. Conclusion

This study presents an evaluation of PFA distribution in Antarctica, utilizing a methodological framework that integrates multiple data sets through a MC approach. Evaluation using OIB data in Greenland demonstrates a 91% correspondence with PFA observations and a 4% incidence of false positives. Similarly, assessment on Wilkins Ice Shelf reveals a 97% detection rate of PFAs identified with MCoRDS data.

The analysis produces a comprehensive PFA heat map, representing the first probabilistic overview of firn PFA locations across Antarctica. Predominantly, PFAs are concentrated within the AP, with elevated probabilities along its northern, northwestern, and western coastlines. The analysis excludes the possibility of PFA presence in the remaining Antarctic regions, except for sporadic occurrences within specific ice shelves, including Abbot, Totten, and Shackleton.

The present probabilistic approach addresses the challenges of PFA distribution in Antarctica's remote environment and offers wider applicability, adept at refining binary maps into probability maps in situations where in-situ confirmation is challenging. The insights derived from these findings contribute to a nuanced understanding of the implications for Antarctic Ice Sheet dynamics. Additionally, the sustained accessibility of freely available C-band and scatterometer observations, complemented by modeling data, facilitates ongoing long-term monitoring of PFA conditions.

Data Availability Statement

The outcomes of the distinct MC tests (2017–2021) for Greenland and the Antarctic Peninsula to reproduce the presented methodology are available on Zenodo (Di Biase, 2024). The script to compute the last day of melt based on ASCAT observations is available in the same repository.

Acknowledgments
V.D.B. acknowledges funding from the Netherlands Earth System Science Center. B.N. was funded by the Fonds de la Recherche Scientifique de Belgique (F.R.S.-FNRS). S.B.M.V. is supported by the Netherlands Organization for Scientific Research (Grant. OCENW.GROOT.2019.091). We acknowledge the National Snow and Ice Data Center QGreenland package, Quantarctica, and the Norwegian Polar Institute for the basemaps utilized in the present work.

References

Ashcraft, I. S., & Long, D. G. (2006). Comparison of methods for melt detection over Greenland using active and passive microwave measurements. *International Journal of Remote Sensing*, *27*(12), 2469–2488. https://doi.org/10.1080/01431160500534465

Banwell, A. F., Datta, R. T., Dell, R. L., Moussavi, M., Brucker, L., Picard, G., et al. (2021). The 32-year record-high surface melt in 2019/2020 on the northern George VI ice shelf, Antarctic Peninsula. *The Cryosphere*, *15*(2), 909–925. https://doi.org/10.5194/tc-15-909-2021

Bevan, S. L., Luckman, A. J., Kuipers Munneke, P., Hubbard, B., Kulessa, B., & Ashmore, D. W. (2018). Decline in surface melt duration on Larsen C Ice Shelf revealed by the advanced scatterometer (ASCAT). *Earth and Space Science*, *5*(10), 578–591. https://doi.org/10.1029/2018EA000421

Brangers, I., Lievens, H., Miège, C., Demuzere, M., Brucker, L., & De Lannoy, G. J. M. (2020). Sentinel-1 detects firn aquifers in the Greenland ice sheet. *Geophysical Research Letters*, *47*(3), e2019GL085192. https://doi.org/10.1029/2019GL085192

Brils, M., Munneke, P. K., Jullien, N., Tedstone, A. J., Machguth, H., van de Berg, W., & van den Broeke, M. (2024). Climatic drivers of ice slabs and firn aquifers in Greenland. *Geophysical Research Letters*, *51*(3), e2023GL106613. https://doi.org/10.1029/2023gl106613

Brodzik, M. J., Billingsley, B., Haran, T., Raup, B., & Savoie, M. H. (2012). EASE-grid 2.0: Incremental but significant improvements for Earth-Gridded data sets. *ISPRS International Journal of Geo-Information*, *1*(1), 32–45. https://doi.org/10.3390/ijgi1010032

Christianson, K., Kohler, J., Alley, R. B., Nuth, C., & van Pelt, W. J. J. (2015). Dynamic perennial firn aquifer on an Arctic glacier. *Geophysical Research Letters*, *42*(5), 1418–1426. https://doi.org/10.1002/2014GL062806

Chu, W., Schroeder, D. M., & Siegfried, M. R. (2018). Retrieval of englacial firn aquifer thickness from ice-penetrating radar sounding in southeastern Greenland. *Geophysical Research Letters*, *45*(21), 11770–11778. https://doi.org/10.1029/2018GL079751

Dall, J., Madsen, S. N., Keller, K., & Forsberg, R. (2001). Topography and penetration of the Greenland ice sheet measured with airborne sar interferometry. *Geophysical Research Letters*, *28*(9), 1703–1706. https://doi.org/10.1029/2000gl011787

da Rosa, K. K., Fernandez, G. B., da Rocha, T. B., Simões, F. L., Vieira, R., & Simões, J. C. (2014). Stratigraphy of Wanda Glacier, King George Island, Antarctica, using ground penetrating radar. *Brazilian Journal of Genetics*, *32*(1), 21–30. https://doi.org/10.22564/rbgf.v32i1.394

de Roda Husman, S., Hu, Z., Wouters, B., Munneke, P. K., Veldhuijsen, S., & Lhermitte, S. (2022). Remote sensing of surface melt on Antarctica: Opportunities and challenges. *Ieee Journal of Selected Topics in Applied Earth Observations and Remote Sensing*, *16*, 2462–2480. https://doi.org/10.1109/JSTARS.2022.3216953

Di Biase, V. (2024). valeriadibiase/FirnAquifers_GRL: Probability of firn aquifer presence in Antarctica by combining remote sensing and regional climate model data - Repository. [Software]. *Zenodo*. https://doi.org/10.5281/zenodo.11479143

Dunn, W. L., & Shultis, J. K. (2011). *Exploring Monte Carlo methods*. Elsevier.

Forster, R. R., Box, J. E., van den Broeke, M. R., Miège, C., Burgess, E. W., van Angelen, J. H., et al. (2014). Extensive liquid meltwater storage in firn within the Greenland ice sheet. *Nature Geoscience*, *7*(2), 95–98. https://doi.org/10.1038/ngeo2043

Fountain, A. G. (1989). The storage of water in, and hydraulic characteristics of, the firn of South Cascade Glacier, Washington State, USA. *Annals of Glaciology*, *13*, 69–75. https://doi.org/10.3189/s0260305500007667

Fountain, A. G., & Walder, J. S. (1998). Water flow through temperate glaciers. *Reviews of Geophysics*, *36*(3), 299–328. https://doi.org/10.1029/97RG03579

Gilbert, E., & Kittel, C. (2021). Surface melt and runoff on Antarctic ice shelves at 1.5°C, 2°C, and 4°C of future warming. *Geophysical Research Letters*, *48*(8), e2020GL091733. https://doi.org/10.1029/2020GL091733

Gorelick, N., Hancher, M., Dixon, M., Ilyushchenko, S., Thau, D., & Moore, R. (2017). Google Earth Engine: Planetary-scale geospatial analysis for everyone. *Remote Sensing of Environment*, *202*, 18–27. https://doi.org/10.1016/j.rse.2017.06.031

Horlings, A. N., Christianson, K., & Miège, C. (2022). Expansion of firn aquifers in southeast Greenland. *Journal of Geophysical Research: Earth Surface*, *127*(10), e2022JF006753. https://doi.org/10.1029/2022JF006753

Hui, F., Ci, T., Cheng, X., Scambo, T. A., Liu, Y., Zhang, Y., et al. (2014). Mapping blue-ice areas in Antarctica using ETM+ and MODIS data. *Annals of Glaciology*, *55*(66), 129–137. https://doi.org/10.3189/2014AoG66A069

Humphrey, N. F., Harper, J. T., & Pfeffer, W. T. (2012). Thermal tracking of meltwater retention in Greenland's accumulation area. *Journal of Geophysical Research*, *117*(F1). https://doi.org/10.1029/2011JF002083

Kuipers Munneke, P., Ligtenberg, S. R. M., van den Broeke, M. R., van Angelen, J. H., & Forster, R. R. (2014). Explaining the presence of perennial liquid water bodies in the firn of the Greenland ice sheet. *Geophysical Research Letters*, *41*(2), 476–483. https://doi.org/10.1002/2013GL058389

Lievens, H., Demuzere, M., Marshall, H.-P., Reichle, R. H., Brucker, L., Brangers, I., et al. (2019). Snow depth variability in the Northern Hemisphere mountains observed from space. *Nature Communications*, *10*(1), 4629. https://doi.org/10.1038/s41467-019-12566-y

Long, D. G., Hardin, P. J., & Whiting, P. T. (1993). Resolution enhancement of spaceborne scatterometer data. *IEEE Transactions on Geoscience and Remote Sensing*, *31*(3), 700–715. https://doi.org/10.1109/36.225536

MacDonell, S., Fernandoy, F., Villar, P., & Hammann, A. (2021). Stratigraphic analysis of firn cores from an Antarctic ice shelf firn aquifer. *Water*, *13*(5), 731. https://doi.org/10.3390/w13050731

Miège, C., Forster, R., Koenig, L., Miller, J., Miller, O., Montgomery, L., et al. (2020). Density, hydrology and geophysical measurements from the wilkins ice shelf firn aquifer. *U.S. Antarctic Program (USAP) Data Center*. https://doi.org/10.15784/601390

Miège, C., Forster, R. R., Brucker, L., Koenig, L. S., Solomon, D. K., Paden, J. D., et al. (2016). Spatial extent and temporal variability of Greenland firn aquifers detected by ground and airborne radars. *Journal of Geophysical Research: Earth Surface*, *121*(12), 2381–2398. https://doi.org/10.1002/2016JF003869

Miller, J. Z., Long, D. G., Jezek, K. C., Johnson, J. T., Brodzik, M. J., Shuman, C. A., et al. (2020). Brief communication: Mapping Greenland's perennial firn aquifers using enhanced-resolution L-band brightness temperature image time series. *The Cryosphere*, *14*(9), 2809–2817. https://doi.org/10.5194/tc-14-2809-2020

Miller, O., Solomon, D. K., Miège, C., Koenig, L., Forster, R., Schmerr, N., et al. (2018). Direct evidence of meltwater flow within a firn aquifer in southeast Greenland. *Geophysical Research Letters*, *45*(1), 207–215. https://doi.org/10.1002/2017gl075707

Ming, A., Rowell, I., Lewin, S., Rouse, R., Aubry, T., & Boland, E. (2021). *Key messages from the ipcc ar6 climate science report (Tech. Rep.)*. Cambridge Centre for Climate Science.

Montgomery, L., Miège, C., Miller, J., Scambos, T. A., Wallin, B., Miller, O., et al. (2020). Hydrologic properties of a highly permeable firn aquifer in the Wilkins ice shelf, Antarctica. *Geophysical Research Letters*, *47*(22), e2020GL089552. https://doi.org/10.1029/2020GL089552

Nienow, P., Sole, A., Slater, D. A., & Cowton, T. (2017). Recent advances in our understanding of the role of meltwater in the Greenland Ice Sheet system. *Current Climate Change Reports*, *3*(4), 330–344. https://doi.org/10.1007/s40641-017-0083-9

Noël, B., van de Berg, W. J., Lhermitte, S., & van den Broeke, M. R. (2019). Rapid ablation zone expansion amplifies north Greenland mass loss. *Science Advances*, *5*(9), eaaw0123. https://doi.org/10.1126/sciadv.aaw0123

Noël, B., van Wessem, J. M., Wouters, B., Trusel, L., Lhermitte, S., & van den Broeke, M. R. (2023). Higher Antarctic ice sheet accumulation and surface melt rates revealed at 2 km resolution. *Nature Communications*, *14*(1), 7949. https://doi.org/10.1038/s41467-023-43584-60

Phillips, T., Rajaram, H., & Steffen, K. (2010). Cryo-hydrologic warming: A potential mechanism for rapid thermal response of ice sheets. *Geophysical Research Letters*, *37*(20). https://doi.org/10.1029/2010GL044397

Poinar, K., Joughin, I., Lilien, D., Brucker, L., Kehrl, L., & Nowicki, S. (2017). Drainage of Southeast Greenland firn aquifer water through crevasses to the bed. *Frontiers in Earth Science*, *5*, 5. https://doi.org/10.3389/feart.2017.00005

Rignot, E., Echelmeyer, K., & Krabill, W. (2001). Penetration depth of interferometric synthetic-aperture radar signals in snow and ice. *Geophysical Research Letters*, *28*(18), 3501–3504. https://doi.org/10.1029/2000gl012484

Scambos, T. A., Fricker, H. A., Liu, C. C., Bohlander, J., Fastook, J., Sargent, A., et al. (2009). Ice shelf disintegration by plate bending and hydro-fracture: Satellite observations and model results of the 2008 Wilkins ice shelf break-ups. *Earth and Planetary Science Letters*, *280*(1–4), 51–60. https://doi.org/10.1016/j.epsl.2008.12.027

Scambos, T. A., Hulbe, C., Fahnestock, M., & Bohlander, J. (2000). The link between climate warming and break-up of ice shelves in the Antarctic Peninsula. *Journal of Glaciology*, *46*(154), 516–530. https://doi.org/10.3189/172756500781833043

Schneider, T. (1999). Water movement in the firn of Storglaciaren, Sweden. *Journal of Glaciology*, *45*(150), 286–294. https://doi.org/10.3189/S0022143000001787

Shang, X., Cheng, X., Zheng, L., Liang, Q., & Chi, Z. (2022). Decadal changes in Greenland ice sheet firn aquifers from radar scatterometer. *Remote Sensing*, *14*(9), 2134. https://doi.org/10.3390/rs14092134

Shi, J., & Dozier, J. (1992). Radar backscattering response to wet snow. *Proceedings IGARSS '92 International Geoscience and Remote Sensing Symposium*, 2, 927–929. https://doi.org/10.1109/IGARSS.1992.578299

Siegert, M., Atkinson, A., Banwell, A., Brandon, M., Convey, P., Davies, B., et al. (2019). The Antarctic Peninsula under a 1.5°C global warming scenario. *Frontiers in Environmental Science*, *7*. https://doi.org/10.3389/fenvs.2019.00102

Simões, J. C., Ferron, F. A., Bernardo, R. T., Aristarain, A. J., StiéVENARD, M., Pourchet, M., & Delmas, R. J. (2004). Ice core study from the king george island, south shetlands, Antarctica. *Pesquisa Antártica Brasileira*, *4*(9–23), 9–23. https://doi.org/10.31789/pab.v4n1.002

Smith, B. (1972). Airborne radio echo sounding of glaciers in the Antarctic Peninsula (Tech. Rep.). *British Antarctic Survey*.

Stiles, W. H., & Ulaby, F. T. (1980). The active and passive microwave response to snow parameters: 1. Wetness. *Journal of Geophysical Research*, *85*(C2), 1037–1044. https://doi.org/10.1029/JC085iC02p01037

Trusel, L. D., Frey, K. E., & Das, S. B. (2012). Antarctic surface melting dynamics: Enhanced perspectives from radar scatterometer data. *Journal of Geophysical Research*, *117*(F2). https://doi.org/10.1029/2011JF002126

Trusel, L. D., Frey, K. E., Das, S. B., Karnauskas, K. B., Kuipers Munneke, P., van Meijgaard, E., & van den Broeke, M. R. (2015). Divergent trajectories of Antarctic surface melt under two twenty-first-century climate scenarios. *Nature Geoscience*, *8*(12), 927–932. https://doi.org/10.1038/ngeo2563

Tsai, Y.-L. S., Dietz, A., Oppelt, N., & Kuenzer, C. (2019). Remote sensing of snow cover using spaceborne SAR: A review. *Remote Sensing*, *11*(12), 1456. https://doi.org/10.3390/rs11121456

van den Broeke, M. (2005). Strong surface melting preceded collapse of Antarctic Peninsula ice shelf. *Geophysical Research Letters*, *32*(12). https://doi.org/10.1029/2005GL023247

van Wessem, J. M., Steger, C. R., Wever, N., & van den Broeke, M. R. (2021). An exploratory modelling study of perennial firn aquifers in the Antarctic Peninsula for the period 1979–2016. *The Cryosphere*, *15*(2), 695–714. https://doi.org/10.5194/tc-15-695-2021

Zheng, L., & Zhou, C. (2020). Comparisons of snowmelt detected by microwave sensors on the Shackleton ice shelf, East Antarctica. *International Journal of Remote Sensing*, *41*(4), 1338–1348. https://doi.org/10.1080/01431161.2019.1666316